Heat transfer enhancement induced by wall inclination in turbulent thermal convection

Saša Kenjereš

Transport Phenomena Section, Department of Chemical Engineering, Faculty of Applied Sciences and J.M. Burgerscentrum for Fluid Mechanics, Delft University of Technology, Julianalaan 136, 2628 BL Delft, The Netherlands

(Received 18 December 2014; revised manuscript received 12 September 2015; published 6 November 2015)

We present a series of numerical simulations of turbulent thermal convection of air in an intermediate range or Rayleigh numbers ($10^6 \leqslant \mathrm{Ra} \leqslant 10^9$) with different configurations of a thermally active lower surface. The geometry of the lower surface is designed in such a way that it represents a simplified version of a mountain slope with different inclinations (i.e., "Λ"- and "V"-shaped geometry). We find that different wall inclinations significantly affect the local heat transfer by imposing local clustering of instantaneous thermal plumes along the inclination peaks. The present results reveal that significant enhancement of the integral heat transfer can be obtained (up to 32%) when compared to a standard Rayleigh-Bénard configuration with flat horizontal walls. This is achieved through combined effects of the enlargement of the heated surface and reorganization of the large-scale flow structures.

DOI: 10.1103/PhysRevE.92.053006 PACS number(s): 44.25.+f, 47.27.T−, 47.55.pb

I. INTRODUCTION

Turbulent thermal convection occurs when a fluid layer is subjected to intensive heating from below and cooling from above in the presence of a gravitational field. This relatively simple geometric configuration served as the paradigm for numerous phenomena of turbulent heat transfer that are ubiquitous in environmental and technological applications, resulting in a large number of theoretical, experimental, numerical, and modeling studies reported in the literature (e.g., Refs. [1–8]). The input nondimensional parameters that define the thermal convection phenomenon are the Prandtl number ($\mathrm{Pr} = \nu/a$, where ν is kinematic viscosity and a is thermal diffusivity), the Rayleigh number ($\mathrm{Ra} = (\beta g \Delta\theta H^3)/(\nu a)$, where β is the thermal expansion coefficient, g is gravitational acceleration, $\Delta\theta$ is the specified temperature difference between horizontal walls, H is the average distance between horizontal walls, and, finally, the geometrical parameter Γ, which is usually defined as the aspect ratio of the domain. The output nondimensional parameter is the Nusselt number defined as $\mathrm{Nu} = (QH)/(\lambda\Delta\theta)$, with Q as the heat-flux density and λ as the thermal conductivity. Two of the issues that remain controversial are the scaling of Nu for very high values of Ra, and the role of large-scale flow structures on heat transfer from the wall. Here we focus on the second issue. It is demonstrated that despite changing the geometry of the setup (cylindrical or rectangular cells and aspect ratio) the heat transfer was practically unaffected [9–11]. Similarly, even in experiments where obstructions within the enclosure were imposed and which changed the mean flow patterns, no significant variation of the heat transfer was observed [12,13]. In contrast to these studies, significant increases in heat transfer were obtained by imposing the local perturbations in boundary layer regions through surface roughness ([14–16], up to 20%) or by imposing additional forcing such as rotation ([17] up 30%) or electromagnetic forcing (up to 70% with a single-magnet–electrode pair [18,19] or more than 500% with multiple-magnet–electrode arrays [20]). The heat transfer enhancement in rectangular cells with imposed regular surface roughness in form of parallelepiped obstacles are analyzed experimentally and numerically in Refs. [21] and [22], respectively. Reference [21] presented a global heat transfer and local temperature measurements and found that a global heat transfer enhancement occurred when the thickness of the boundary layer matched the height of the roughness. In their Direct Numerical Simulation (DNS) studies, the authors of Ref. [22] also found that the heat transfer increase was obtained by changing the obstacle height and the distance between the obstacles. These changes imposed different ventilation effects in the space between the obstacles, which resulted in more efficient heat transfer when compared to a smooth wall case.

An interesting study was presented in Ref. [23] in which heat transfer enhancement was obtained (up to 17%) for water in an intermediate range of Ra ($8.6 \times 10^7 \leqslant \mathrm{Ra} \leqslant 2.5 \times 10^9$) by gradually reducing width to height aspect ratios (W/H) from 0.6 to 0.1. This was the first study which directly confirmed that changes in the bulk flow can influence dynamics of the boundary layers and, consequently, increase heat transfer. In the present work, we continue investigations of the possibility that changes in the large-scale flow structures can significantly affect heat transfer. Motivated with the idea of persistent up- or down-slope air motion in hilly or mountain regions (so-called anabatic or katabatic winds, respectively), such as are generated during diurnal (day-night) cycles ([24–27]), we will impose different inclinations of the lower surface. We assume that such inclinations will be able to redirect the main large-scale circulation even when wall temperature is kept constant. We will investigate whether such generated fluid motion can produce an enhancement of heat transfer enhancement comparable to the situation with the flat walls.

II. METHOD

A. Equations and large-eddy simulation (LES) subgrid closures

We apply the large-eddy simulation (LES) approach for which the governing equations of mass, momentum, and energy are introduced for the case of the nonorthogonal coordinate system as follows:

$$\frac{\partial \rho}{\partial t} + \frac{1}{J}\frac{\partial}{\partial y^j}\left(\rho v_m \beta_m^j\right) = 0, \tag{1}$$

$$\frac{\partial(\rho v_i)}{\partial t}+\frac{1}{J}\frac{\partial}{\partial y^j}\left[(\rho v_m v_i - T_{mi})\beta_m^j\right]=S_{v_i}, \quad (2)$$

$$\frac{\partial(\rho\theta)}{\partial t}+\frac{1}{J}\frac{\partial}{\partial y^j}\left[(\rho v_m \theta - q_m)\beta_m^j\right]=S_\theta. \quad (3)$$

Here ρ, v_i, and θ are the fluid density, the resolved velocity vector, and temperature (here an active scalar), respectively. The S_{v_i} and S_θ represent the source terms in momentum and temperature equations. The β_m^j represents the cofactor of $\partial x^i/\partial y^j$ in the Jacobian (J) of the coordinate transformation $x^i = x^i(y^j)$, with $(y^1,y^2,y^3)=(\xi,\eta,\zeta)$ and $(x^1,x^2,x^3)=(x,y,z)$ as a general curvilinear and the reference Cartesian coordinate system, respectively [28]. The T_{mi} and q_m are the stress tensor and heat flux vector, expressed as:

$$T_{mi}=\frac{1}{J}\mu\left(\frac{\partial v_i}{\partial y^n}\beta_m^n+\frac{\partial v_m}{\partial y^l}\beta_i^l\right)-\rho\overline{v_i v_m}, \quad (4)$$

$$q_m=\frac{1}{J}a\left(\frac{\partial\theta}{\partial y^n}\beta_m^n\right)-\rho\overline{\theta v_m}, \quad (5)$$

where μ and a are the dynamic viscosity and thermal diffusivity, respectively. The unresolved subgrid turbulent stress ($\overline{v_i v_m}$) and subgrid turbulent heat flux vector ($\overline{\theta v_m}$) need to be provided to get fully closed system of equations. By assuming a weak compressibility of the fluid through the Boussinesq approximation and that there is no internal heat generation, the final form of the governing equations, now written in the Cartesian coordinate system (in order to simplify writing of the vectorial and tensorial components), follows as:

$$\frac{\partial u_i}{\partial x_i}=0, \quad (6)$$

$$\frac{\partial u_i}{\partial t}+u_j\frac{\partial u_i}{\partial x_j}=-\frac{1}{\rho_0}\frac{\partial p}{\partial x_i}-\beta g_i(\theta-\theta_0)+\frac{\partial}{\partial x_j}\left[\nu\left(\frac{\partial u_i}{\partial x_j}+\frac{\partial u_j}{\partial x_i}\right)-\tau_{ij}\right], \quad (7)$$

$$\frac{\partial\theta}{\partial t}+u_j\frac{\partial\theta}{\partial x_j}=\frac{\partial}{\partial x_j}\left(a\frac{\partial\theta}{\partial x_j}-\tau_{\theta j}\right), \quad (8)$$

where θ_0 is the referent temperature.

To make the numerical approach computationally effective, because several configurations need to be considered, and, finally, because the long-term averaged first- and second-flow statistics need to be analyzed, we adopt a wall-resolved LES approach. In the present study, we use the subgrid turbulent stress closure of Ref. [29]. We selected this model since it previously proved to perform well in cases where flow regimes can coexist within a single simulation domain and because of the fact that it properly mimics the near-wall behavior of the turbulent viscosity without any additional damping functions. As reported in Ref. [29] this model was tested for cases that included a developing mixing layer and a fully developed turbulent channel flow and produced results in close agreement with a dynamic Smagorinsky model. In contrast to the dynamic Smagorinsky model, this model does not require any form of local averaging or averaging in homogeneous flow directions, which makes it numerically effective. The subgrid turbulent stress (τ_{ij}) and subgrid turbulent viscosity (ν_t) in model of Ref. [29] can be written as:

$$\tau_{ij}=-\nu_t\left(\frac{\partial u_i}{\partial x_j}+\frac{\partial u_j}{\partial x_i}\right)+\frac{1}{3}\overline{u_k u_k}\delta_{ij},$$

$$\nu_t=c\sqrt{\frac{B_\beta}{\alpha_{ij}\alpha_{ij}}},\quad \alpha_{ij}=\partial u_j/\partial x_i,\quad \beta_{ij}=\Delta_m^2\alpha_{mi}\alpha_{mj}, \quad (9)$$

$$B_\beta=\beta_{11}\beta_{22}-\beta_{12}^2+\beta_{11}\beta_{33}-\beta_{13}^2+\beta_{22}\beta_{33}-\beta_{23}^2,$$

where $c=0.07$ and $\nu_t=0$ when $B_\beta<10^{-8}$. The Δ_m are the filter-length projections of the characteristic control volume onto Cartesian coordinates. The subgrid turbulent heat flux is calculated using a simple-gradient diffusion hypothesis (SGDH) as:

$$\tau_{\theta i}=-a_t\frac{\partial\theta}{\partial x_i}, \quad (10)$$

where the subgrid turbulent thermal diffusivity is $a_t=\nu_t/\mathrm{Pr}$, with ν_t from Eq. (9) and $\mathrm{Pr}=0.4$, as used in Refs. [20,30,31].

B. Numerical method

The discretized forms of Eqs. (6)–(10) are solved by our in-house finite-volume numerical code for the nonorthogonal geometries. The control volumes are in the form of hexahedra. We use a collocated grid arrangement, i.e., all transport variables are located in the geometrical centers of control volumes. The Cartesian vector and tensor components are used on the boundary-fitted coordinates [Eqs. (1)–(5)]. To prevent a decoupling between the velocity and pressure fields, the Rhie-Chow interpolation is used in the pressure-correction equation within the semi-implicit method for pressure-linked equations (SIMPLE) algorithm. Both convective and diffusive terms in the discretized form of the transport equations are calculated by the second-order central-differencing (CDS) scheme. The fully implicit three-time-level second-order scheme is used for time integration. For more details on the numerical method used, see Refs. [18,20,31–34].

C. Geometry of the setup and boundary conditions

We select air as the working fluid ($\mathrm{Pr}=0.71$) and address a range of Ra ($10^6\leqslant \mathrm{Ra}\leqslant 10^9$) for different inclinations of the lower surface, Fig. 1. The horizontal top surface is kept flat, whereas the bottom surface is varied to produce the "V"- (or "Λ"-) shaped topologies with different inclination angles, i.e., different h/H ratios of 0, 0.125, 0.25, 0.35, 0.5, 0.65, 0.75, 0.85, and 0.95 (which give a characteristic angle of inclination $0^\circ\leqslant\alpha\leqslant 43.5^\circ$), respectively. The overall aspect ratio of the box (L:W:H = 4:4:1) is also kept constant. The lower and upper boundaries have fixed temperatures of θ_h and θ_c, respectively, and the remaining vertical side walls are adiabatic. The referent temperature is calculated as $\theta_0=(\theta_h A_{\mathrm{bottom}}+\theta_c A_{\mathrm{top}})/(A_{\mathrm{bottom}}+A_{\mathrm{top}})$, where A_{bottom} and A_{top} are surface areas of bottom and top boundary, respectively. The no-slip condition is imposed at all boundaries.

Numerical meshes containing $182^2\times 102$ (for $\mathrm{Ra}\leqslant 10^8$) and $256^2\times 182$ (for $\mathrm{Ra}>10^8$) are used for simulations. The numerical mesh is refined in the near-wall regions such that it properly resolves hydrodynamic and thermal boundary layers (wall-resolving LES applies here [7]). The near-wall mesh

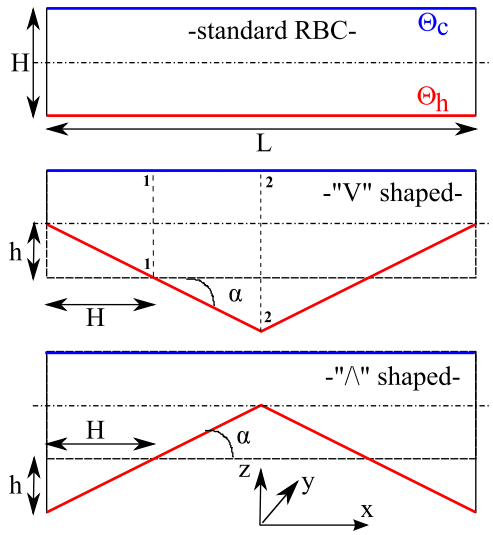

FIG. 1. (Color online) Sketch of the configurations under study: flat (top), "V" inclined (middle), and "Λ" inclined (bottom). Different inclinations of the lower surface are obtained by varying the ratio $h/H = 0$, 0.125, 0.25, 0.35, 0.5, 0.65, 0.75, 0.85, and 0.95. The bottom and top boundaries are kept at constant temperatures, θ_h and θ_c, respectively, whereas all side walls are kept adiabatic. The overall constant aspect ratio of $(L{:}W{:}H = 4{:}4{:}1)$ is kept for all cases.

refinement is defined to give nondimensional wall distances for the very first rows of control volumes of $x_1^{+n} \approx 0.5$ and $\Delta \approx (1-2)\eta_k$, whereas $\Delta \approx (5-10)\eta_k$ in the center of the enclosure (where η_k is the Kolmogorov length scale). The characteristic time step is specified such that the maximal value of the Courant-Friedrichs-Lewy number is 0.5.

III. RESULTS AND DISCUSSION

A. Instantaneous flow and thermal field features

To portray the most salient flow features for different configurations, we plotted the side views of thermal plumes [projections into two-dimensional planes, i.e., the $(x\text{-}z)$ plane, Fig. 2 (left), and the $(y\text{-}z)$ plane, Fig. 2 (right)], which are identified as isosurfaces of instantaneous temperatures $\{[\theta^* = \theta/(\theta_h - \theta_c) = 0.675$ [hot (red)] and 0.325 [cold (blue)]$\}$. For the configuration with flat horizontal walls at $\mathrm{Ra} = 10^7$ [Fig. 2 (top)], intermittent meanderings of thermal plumes impose strong vertical shear and generate well-defined large convective structures (cells and rolls). Changes in the lower boundary inclination induce significant spatial reorganization of instantaneous thermal plumes. For the "V"-shaped configuration, the lower boundary inclination imposes up-slope flow motion, which, after reaching the vertical side walls, is transferred into distinct vertical updraft motion. In contrast to that, for the "Λ-shaped" case, the vertical impingement region is in the central part of the enclosure, where two up-slope moving jets collide. Similar behavior of thermal plumes is also observed for higher Rayleigh numbers [10^9, Fig. 2 (bottom)], but significantly finer thermal plume structures are observed for all configurations. That thermal plumes thin with an increase of Ra was also observed both experimentally (e.g., Refs. [35,36]) and numerically (e.g., Refs. [37–40]) for the configuration with flat horizontal walls.

The presence of large convective structures is visible on plots of instantaneous stream traces in characteristic central $(x\text{-}z$ and $y\text{-}z)$ vertical planes for the "V_0.75" and "Λ_0.5" configurations at $\mathrm{Ra} = 10^7$, Fig. 3 (left). In characteristic vertical $(y\text{-}z)$ plane cross sections, imprints of the vortical structures are mainly focused in the proximity of the lower boundary for the "V_0.75" configuration and in the proximity of the upper boundary for the "Λ_0.5" configuration, as seen in Fig. 3 (bottom). These correspond to the impingement regions of vertical down-drafts (for the "V_0.75") and up-drafts (for the "Λ_0.5") where, due to strong inertia and a sudden change in the flow direction, the low-pressure regions and strong vortical flow structures are generated. From the instantaneous temperature fields [Fig. 3 (right)] it can be seen that predominantly cold (hot) plumes are occupying the upper (lower) parts of the characteristic vertical planes for the "V_0.75" and "Λ_0.5" configurations.

The time evolutions of the Nusselt numbers for configurations with both boundaries flat and with corresponding maximally inclined configuration ("V_0.95") are shown in Fig. 4 (left) for two different values of Ra $\{10^6$ [Fig. 4 (top)] and 10^8 [Fig. 4 (bottom)]$\}$. We can deduce two things from these plots: that the wall-heat transfer is in a statistically steady mode (also note that we here present only 1/5 of the total long-term time-averaged cycle that was used for evolutions of the total integral heat transfer and of the second-order statistics) and that the wall inclination produced significant heat transfer enhancement (up to ≈25%) for cases presented here. The heat transfer enhancement will be addressed in more detail in the follow-up section.

The time evolutions of the ratio between the turbulent subgrid and molecular viscosity $(\nu_t^{\mathrm{SGS}}/\nu)$ for two characteristic locations (in the proximity of the upper-cold boundary and in the enclosure center) are presented in Fig. 4 (right). This ratio displays the significance of the contribution of unresolved turbulence. As expected, the more intermittent behavior is obtained for the higher Ra, Fig. 4 (bottom right). For both cases ($\mathrm{Ra} = 10^6$ and 10^8), at the near-wall location (indicated by red lines), instantaneous and time-averaged values are well below 1, demonstrating the fully resolved simulations in the proximity of solid boundary due to the numerical mesh clustering employed in the vertical direction. The situation differs for the location at the enclosure center (blue lines), where this ratio is still well below 1 for $\mathrm{Ra} = 10^6$, whereas for $\mathrm{Ra} = 10^8$, this ratio reaches values up to 5. This is also expected, since a coarser numerical mesh is used in the central part of the enclosure where the subgrid turbulence contribution is significant.

B. The long-term time-averaged wall heat transfer

Next, we focus on the analysis of the time-averaged quantities. The long-term time averaging is performed over 10^5 instantaneous fields. The duration of the time interval used to collect the long-time averaged statistics is selected such that it resolves at least 100 characteristic turnover convective time scales (t/T_0). This is significantly larger than in Ref. [37] or Ref. [41] where only 1 and 5 characteristic convective turnover

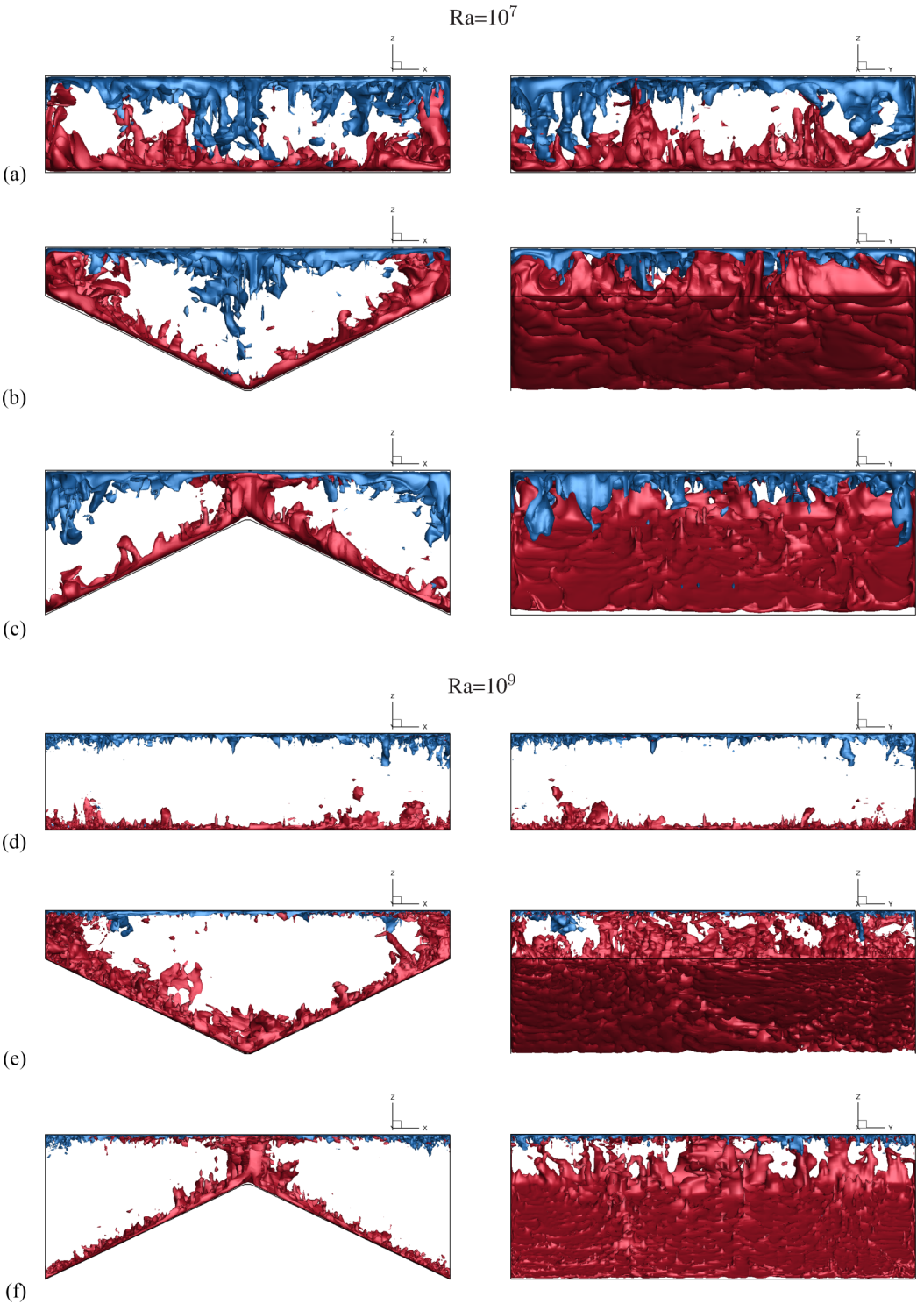

FIG. 2. (Color online) The side views [left (x-z) plane and right (y-z) plane] of the instantaneous thermal plumes identified as $\theta^* = 0.675$ (red) and 0.325 (blue) for different configurations {flat walls [(a) and (d)], "V_0.75" [(b) and (e)], and "A_0.5" [(c) and (f)]} at Ra [10^7 (top) and 10^9 (bottom)] where $\theta^* = (\theta - \theta_c)/\Delta\theta$ and $\Delta\theta = (\theta_h - \theta_c)$.

times were resolved for the highest simulated values of Ra, 2×10^7 and 10^8, respectively.

The total time-averaged Nusselt numbers at the top boundary for different values of Ra and different lower boundary inclinations are shown in Fig. 5. We also plotted some additional DNS and LES results from the literature for a standard configuration with both horizontal walls flat (also shown in Table I). To illustrate the level of agreement with the spectral DNS results for classical Rayleigh-Bénard case (flat horizontal walls), we compare our results with Refs. [37] and [41]. In Ref. [37], the least-square fit of DNS results is proposed as $\mathrm{Nu} = 0.186\mathrm{Ra}^{0.276}$ for a high-aspect ratio

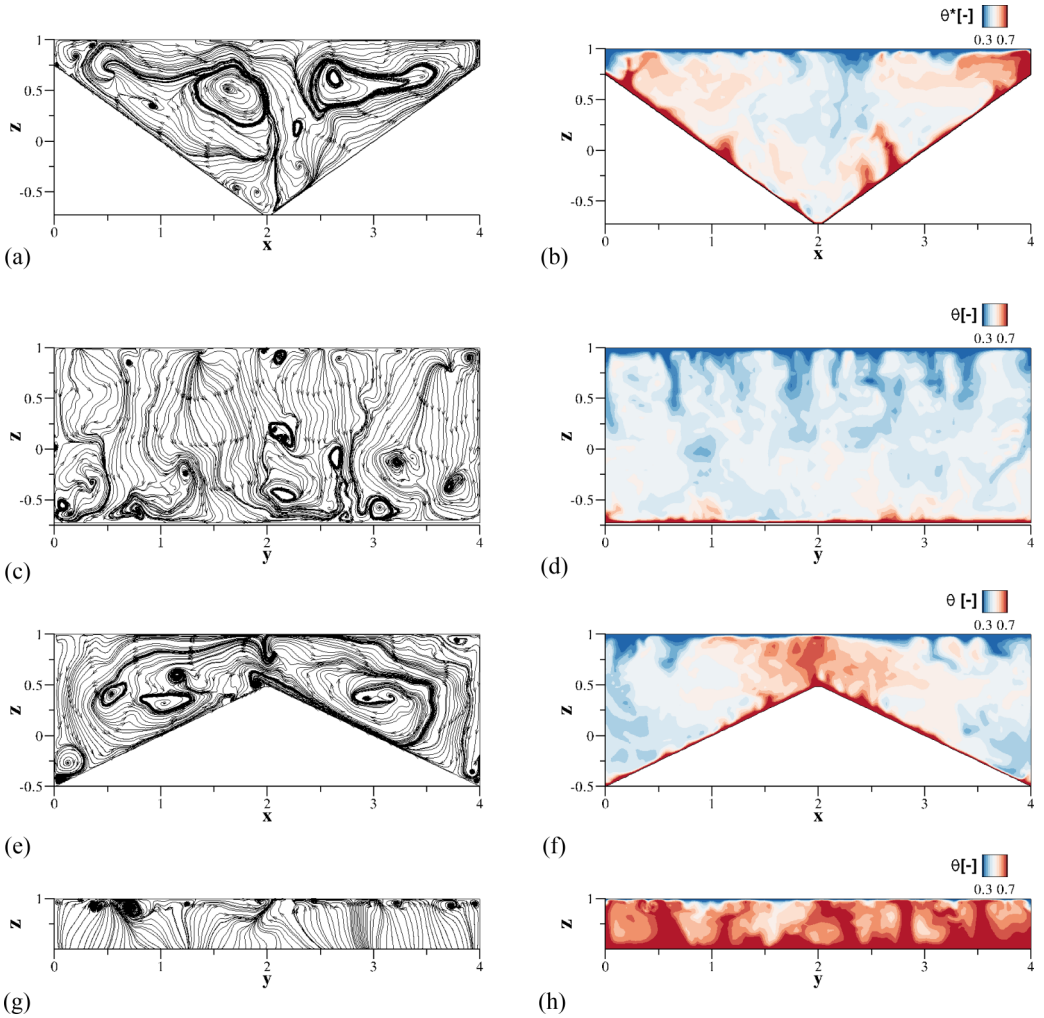

FIG. 3. (Color online) Instantaneous stream traces (left) (calculated from the resolved velocity field) and temperature (right) in the central (x-z) [(a), (b), (e), and (f)] and (y-z) [(c), (d), (g), and (h)] planes for "V_0.75" [(a)–(d)] and "Λ_0.5" [(e)–(h)] configurations, both at Ra $= 10^7$.

domain (L:W:H = 6:6:1) in the $5 \times 10^4 \leqslant \mathrm{Ra} \leqslant 2 \times 10^7$ range and Pr = 0.7. Numerical meshes up to $288^2 \times 96$ were used. Similarly, Ref. [41] presented results of spectral DNS for a (L:W:H = 4:4:1) aspect ratio enclosure with periodic side boundaries in the $1.15 \times 10^5 \leqslant \mathrm{Ra} \leqslant 10^8$ range. The employed numerical mesh varied as $128^2 \times 64$, $192^2 \times 128$, 256^3, and $640^2 \times 320$ for Ra $= 1.15 \times 10^5$, 10^6, 10^7, and 10^8, respectively. Our values of Nu agree well with both spectral DNS results for Ra $= 10^6$ and 10^7 (with maximal differences of 3% and 1%, respectively). For higher values of Ra, we compare our results with LES of Refs. [42] and [43]. The LES of Ref. [42] were performed by using a dynamic mixed scale diffusivity subgrid model with meshes up to $128^2 \times 112$ in large-aspect ratio domains (L:W:H = 6:6:1 and L:W:H = 4:4:1) in the $2 \times 10^6 \leqslant \mathrm{Ra} \leqslant 2 \times 10^{10}$ range. The correlation $\mathrm{Nu} = 0.131\mathrm{Ra}^{0.302}$ was proposed for Pr = 0.7. The LES results presented agree well with Ref. [42] (with maximal difference of 3.5% in $10^8 \leqslant \mathrm{Ra} \leqslant 10^9$ range). The difference is higher (max. difference of 10%) when compared with LES of Ref. [43] for highest value of Ra = 10^9, where the (6:6:1) aspect ratio domain was simulated in the $6.5 \times 10^5 \leqslant \mathrm{Ra} \leqslant 10^9$ range and a $\mathrm{Nu} = 0.162\mathrm{Ra}^{0.286}$ correlation was proposed. This difference can be explained in terms of a coarser numerical mesh $176^2 \times 128$ applied over a larger aspect ratio domain (6:6:1) (especially for the two largest Ra numbers) and a relatively short time-averaging interval of 12 characteristic convective time scales, which was used to calculate the averaged Nu (as specified in Ref. [43]). Based on all comparisons of the averaged Nu presented above, we conclude that an overall good agreement is obtained in predicting averaged integral heat transfer for the standard Rayleigh-Bénard convection in a range of Ra.

Now we will address how different inclinations of the bottom boundary affect the integral heat transfer. It is demonstrated already in Fig. 5 that steeper inclinations produce more intensive heat transfer compared to the flat walls. The heat transfer enhancement ($\mathrm{Nu}/\mathrm{Nu}_0$) for all configurations considered here is shown in Fig. 6. The double horizontal axes indicate the ratios between the thermally active area (total or just of the bottom boundary) for inclined configuration and configuration with flat walls. The maximum ratios of $(A/A_0)_{\mathrm{total}}$ and $(A/A_0)_{\mathrm{bottom}}$ reach values of 1.2 and

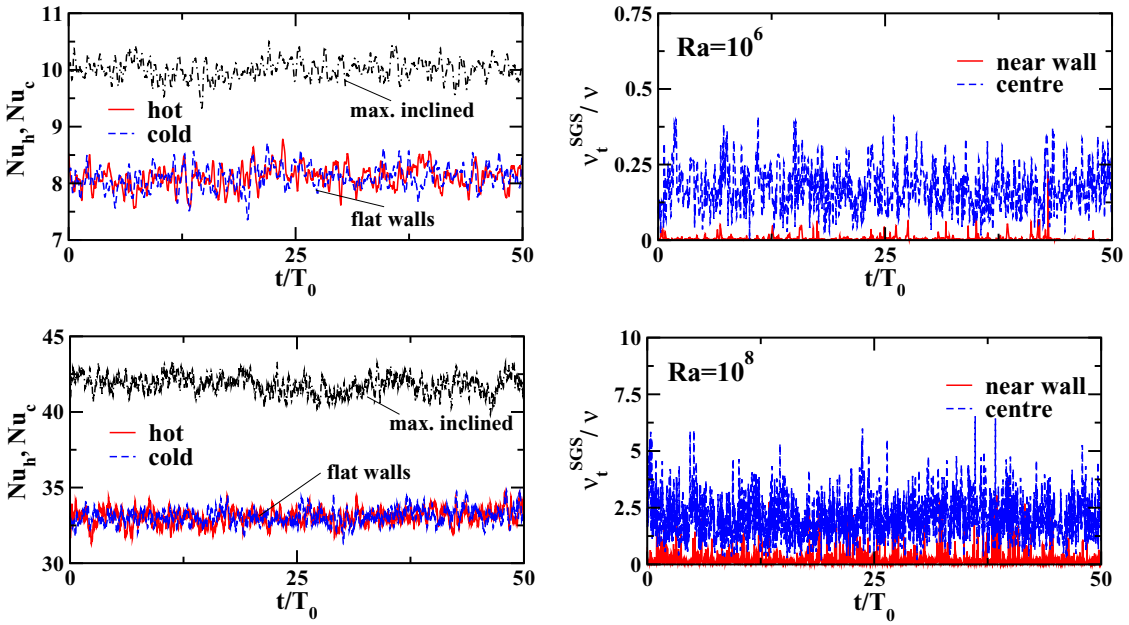

FIG. 4. (Color online) Time evolutions of the Nusselt number (Nu_h and Nu_c) (left) and of the ratio between the turbulent subgrid and molecular viscosity (ν_t^{SGS}/ν) (right) for two values of Ra [10^6 (top) and 10^8 (bottom)]. The $T_0 = H/u_0$ is the characteristic convective time scale, where $u_0 = (\nu\beta g\Delta\theta)^{1/3}$.

1.4, respectively, for the steepest configuration considered ("V_0.95").

An increase of Nu is observed for all inclined configurations, Fig. 6. The maximal heat transfer enhancement (Nu/Nu_0) of 32% is obtained for the highest $Ra = 10^9$ with the steepest inclination, "V_0.95." This overall increase in Nu is not just a simple consequence of the enlargement of the heating area (given as the ratio between surface areas for inclined and flat walls, A/A_0). If this would be the case, the heat transfer enhancement (Nu/Nu_0) would be independent of Ra for a fixed value of (A/A_0). By contrast, we observe a strong Ra dependency. This is our first evidence that a flow reorganization also contributes to the wall-heat transfer enhancement. When comparing heat transfer enhancement to the total thermally active area $(A/A_0)_{total}$ (dashed red-line in Fig. 6), we observe that all values of (Nu/Nu_0) lay above this line. For the lowest $Ra = 10^6$ and configurations "V_0.35," "V_0.50," and "V_0.65," the (Nu/Nu_0) slope follows closely the slope of $(A/A_0)_{total}$. A similar trend is observed for the three highest $Ra = 10^8$, 5×10^8, and 10^9 and "V_0.75," "V_0.85," and "V_0.95" configurations. With respect to the $(A/A_0)_{bottom}$ line, which indicates only area enlargement of the heated surface (blue dashed-dot line in Fig. 6), the only (Nu/Nu_0) points above this line are obtained for smaller angles of inclination (from "V_0.125" to "V_0.65") and highest values of $Ra = 5 \times 10^8$ and 10^9. So far, we analyzed only configurations with the "V-type" inclinations. We performed two additional simulations with a "Λ_0.5" configuration, for $Ra = 10^7$ and 10^9. The heat transfer enhancement (Nu/Nu_0) obtained is 1.066 and 1.188 for $Ra = 10^7$ and 10^9, respectively. When compared with the heat transfer enhancement (Nu/Nu_0) for the "V_0.5"

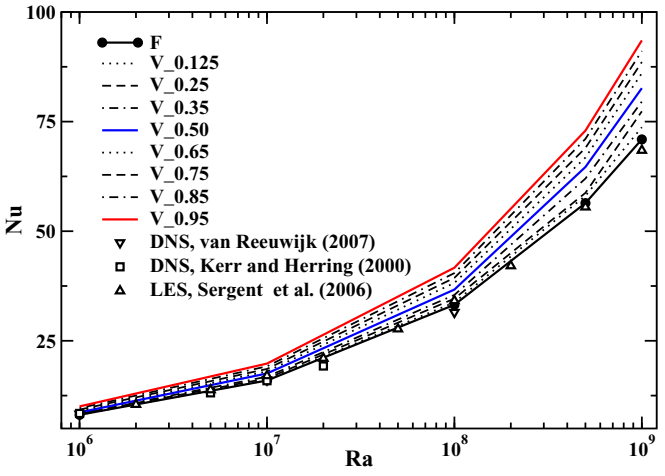

FIG. 5. (Color online) The long-term time-averaged total Nusselt number at the top boundary for different values of Ra ($10^6 \leqslant Ra \leqslant 10^9$) and different configurations of the bottom boundary [starting with flat (F) to different V-type inclinations]. The symbols are results (spectral DNS and LES) from literature for basic (flat walls) configurations with large aspect ratios and Pr = 0.71, which are also used in the present study.

TABLE I. Integral heat transfer (Nusselt number) for a standard Rayleigh-Bénard convection of air in enclosures with large aspect ratios.

Ra =	10^6	10^7	10^8	5×10^8	10^9
DNS of Ref. [37]	8.42	15.9	—	—	—
DNS of Ref. [41]	8.3	16.1	31.1	—	—
LES of Ref. [42]	—	17.03	34.14	55.5	68.43
LES of Ref. [43]	8.42	16.27	31.44	49.82	60.75
Present	8.12	15.96	33.2	56.4	70.95

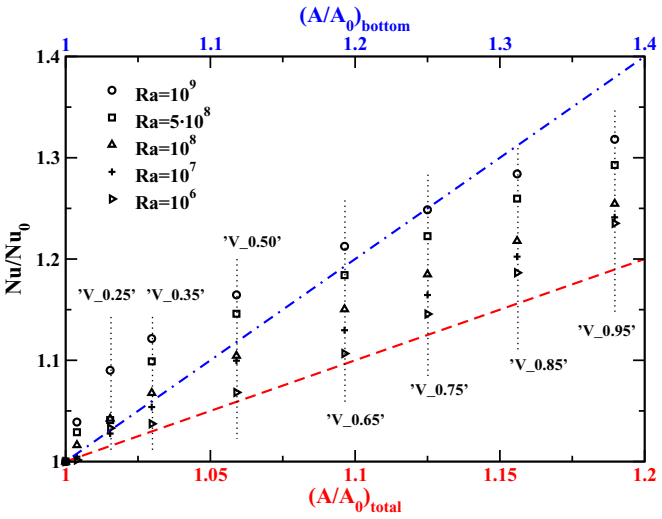

FIG. 6. (Color online) The heat transfer enhancement (Nu/Nu_0) as function of ratios of the enlarged (inclined) and basic (flat) thermally active areas [the total area, $1 \leqslant (A/A_0)_{total} \leqslant 1.2$; only the bottom boundary, $1 \leqslant (A/A_0)_{bottom} \leqslant 1.4$, where A_0 is the area for configuration with both flat walls] for all considered situations.

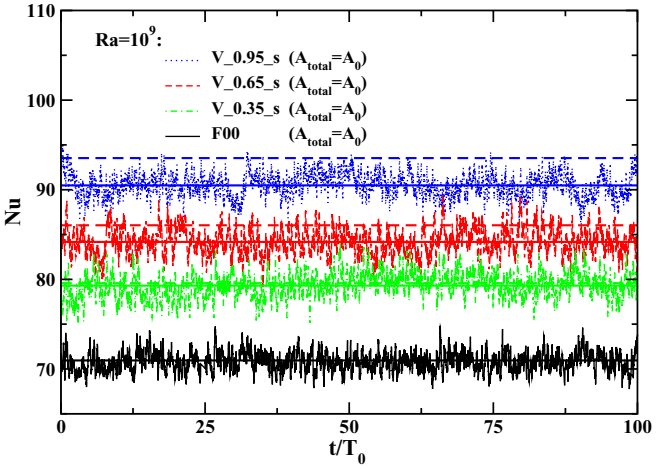

FIG. 7. (Color online) The time evolution of the integral heat transfer (Nusselt number) at the upper boundary at $Ra = 10^9$ with some selected inclinations ("V_0.95," "V_0.65," and "V_0.35") but now with rescaled total thermally active surfaces to be identical to the total active area (A_0) of configuration with flat boundaries ("F_00"). The solid lines represent the long-term time-averaged values for such rescaled inclined geometries (i.e., $A_{total} = A_{top} + A_{bottom} = A_0$), whereas dashed lines are the original configurations with inclinations.

configuration of 1.098 and 1.165 for $Ra = 10^7$ and 10^9, respectively, relatively small differences are observed. To summarize, significant heat transfers (more than 10%) are obtained for all simulated values of Ra, starting with an inclination configuration "V_0.65." This 10% increase is easily reached even with relatively modest inclinations ("V_0.35") for the two highest Ra numbers considered, $Ra = 5 \times 10^8$ and 10^9.

To provide more detailed insight into separate contributions of flow reorganization and augmented surface area on the heat transfer enhancement, we focus on the $Ra = 10^9$ case where a highest heat transfer enhancement is obtained. Here we select three configurations with inclinations: the highly, moderately, and slightly inclined bottom boundary. These configurations are now rescaled to obtain an identical total thermally active surface areas as for the neutral case (A_0), i.e., the configuration with flat boundaries ("F_00"). This rescaling is performed by keeping identical projection in the vertical (x-z) plane and the spanwise extension (in the y direction) is properly adjusted. If there will be no effects of the flow reorganization, the integral heat transfer will be identical for all four cases. The time evolutions of the Nusselt number for such rescaled geometries are shown in Fig. 7. The solid and dashed straight lines indicate the long-term time-averaged Nusselt values for the rescaled and original configurations, respectively. It can be seen that the significant heat transfer enhancement is still present for all inclined configurations. The differences between the values characterized by solid lines for inclined configurations and referent ("F_00") case indicate Nusselt number increase by the flow reorganization. The remaining differences with corresponding dashed lines are contributions of the effective thermally active surface enlargement. We obtain Nu/Nu_0 values of 1.12, 1.186, and 1.275 for the rescaled 'V_0.35_s," "V_0.65_s," and "V_0.95_s" configurations, respectively. By comparing these values with values presented in Fig. 6 for the nonscaled counterparts for identical inclinations, where Nu/Nu_0 of 1.121, 1.21, and 1.32 are obtained, we conclude that the flow reorganization is the major contributor to the heat transfer increase for high Ra.

Now we compare levels of the heat transfer enhancement achieved here with a few similar studies reported in literature. Comparable heat transfer enhancements (up to 17% and 11% for $Ra = 8.6 \times 10^7$ and 2.5×10^9, respectively, and $Pr = 4.3$) are observed for Rayleigh-Bénard convection with flat walls due to confinement effects [23]. In contrast to the work of Ref. [17], where no enhancement at all was obtained with system rotation for working fluid with $Pr = 0.7$, and of Ref. [23], where the Nu increase was reduced with Ra increase, we find more efficient heat transfer as Ra increases.

As the next step, we analyze local distributions of the time-averaged Nusselt number at the top horizontal boundary, Fig. 8. A diagonally symmetric distribution is obtained with a configuration with flat walls for both Ra, Fig. 8 (top). In contrast, configurations with lower boundary inclinations show characteristic peaks in the proximity of the side walls (for "V"-shaped ones) [Fig. 8 (middle] or in the center of the box (for "Λ"-shaped ones) [Fig. 8 (bottom)]. This distribution confirms that an imposed wall inclination predetermines the locations where vertical ejections of the hot thermal plumes will take place. This is in contrast with the configuration with both flat walls where the vertical up-drafts and down-drafts are randomly distributed over the heated and cooled surfaces. For configurations with inclined walls, the double symmetry of Nu distributions in respect to the $x/L = 2$ and $y/W = 2$ lines [Figs. 8 (left middle) and 8 (left bottom)] is reduced to the single line of symmetry $x/L = 2$, with Ra number increase [Figs. 8 (right middle) and 8 (right bottom)].

C. The long-term time-averaged flow and temperature fields

To investigate a possible association of the enhancement of heat transfer with reorganization of large flow structures,

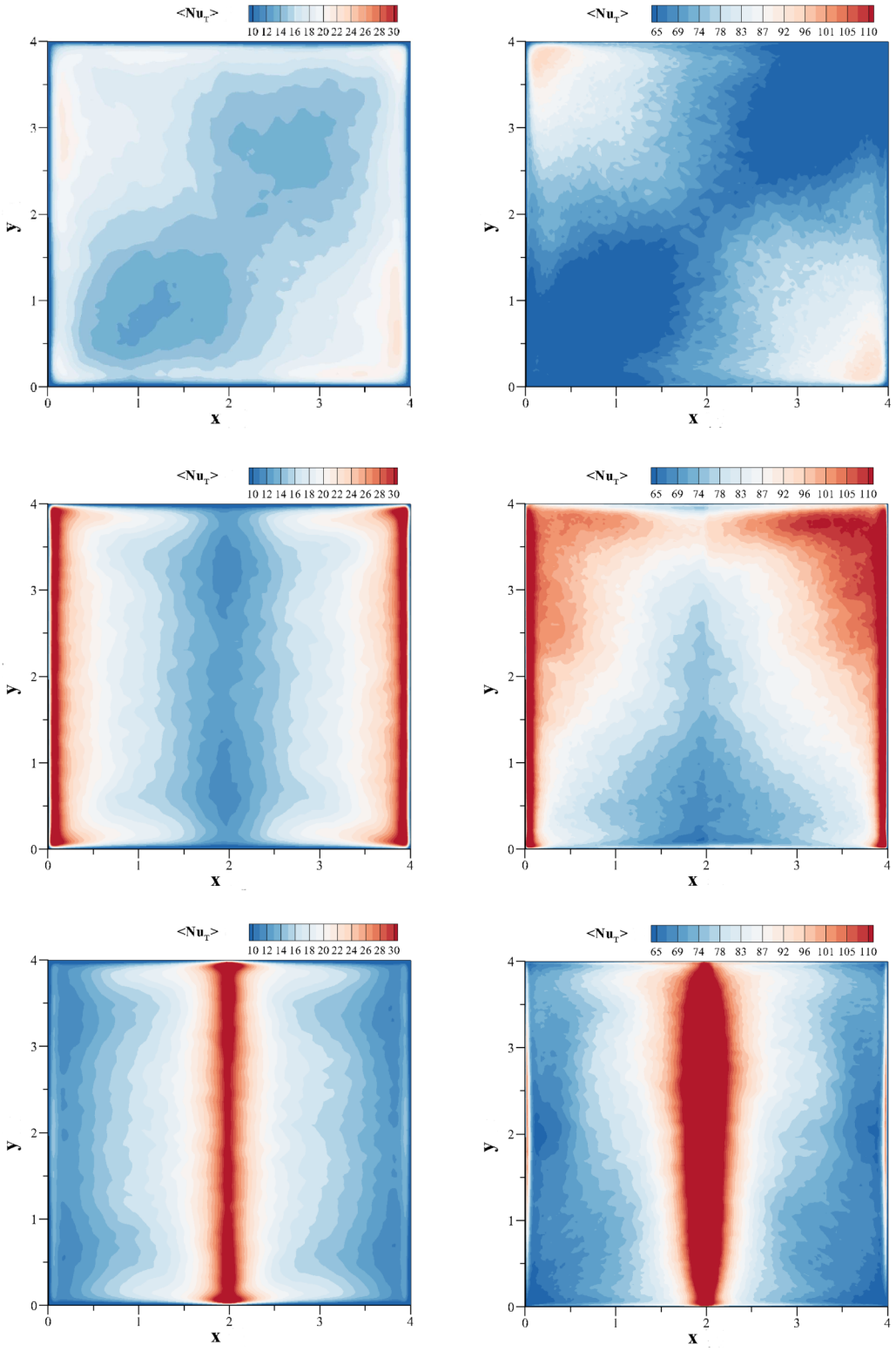

FIG. 8. (Color online) The contours of the long-term time-averaged local Nusselt number at the top boundary for different configurations ["F" (top); "V_0.75" (middle); "Λ_0.5" (bottom)] and two values of Ra [10^7 (left) and 10^9 (right)].

we analyze next the time-averaged velocity and temperature fields (both first- and second-order moments). The characteristic stream traces and contours of the velocity components (horizontal and vertical), as well as of the turbulent kinetic energy and temperature variance, in the central vertical plane for the "V_0.75" and "Λ_0.5" configurations, at Ra = 10^7, are shown in Figs. 9 and 10, respectively. The stream traces depict the multicellular patterns with single pairs of the central convective and small upper-corner structures for the "V_0.75" configuration, Fig. 9 (top). For the "Λ_0.5" configuration, two

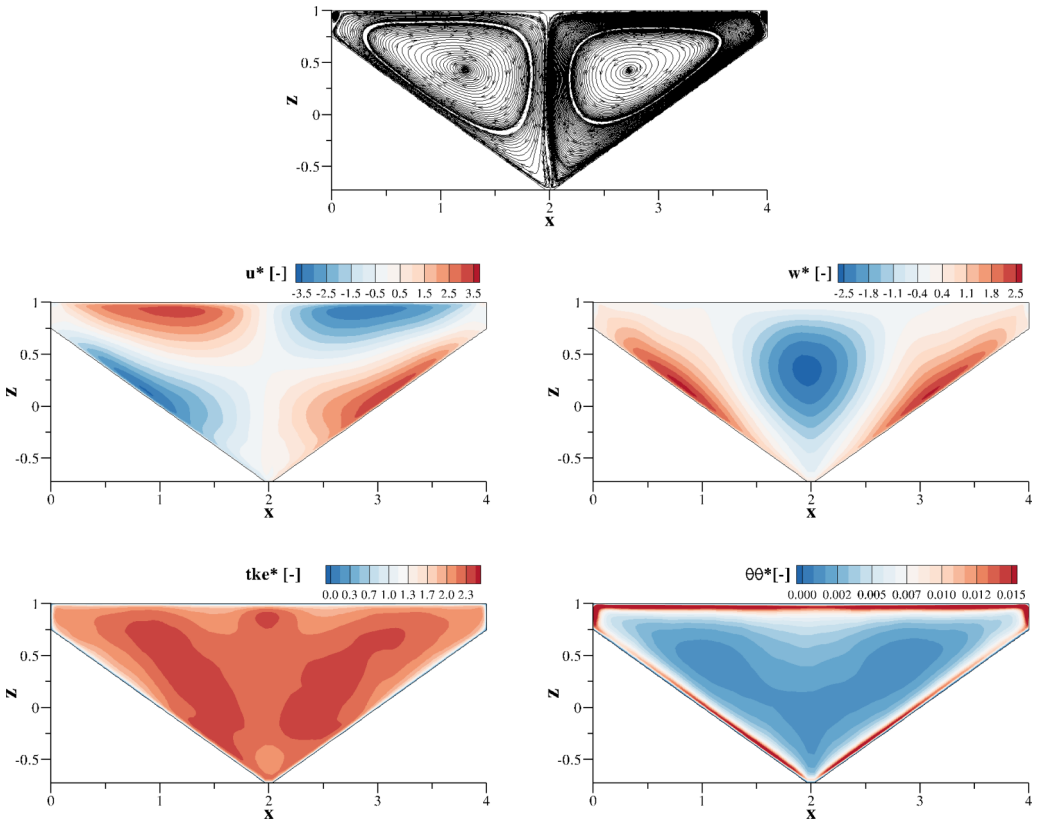

FIG. 9. (Color online) The long-term time-averaged stream traces (top), mean horizontal ($u^* = \overline{u}/u_0$) and vertical ($w^* = \overline{w}/u_0$) velocity components (middle), turbulent kinetic energy ($tke^* = \sqrt{0.5(\overline{uu} + \overline{vv} + \overline{ww})}/u_0$), and temperature variance ($\theta\theta^* = \sqrt{\overline{\theta^2}}/\Delta\theta$) (bottom) in the central vertical cross section for the "V_0.75" configuration at Ra $= 10^7$.

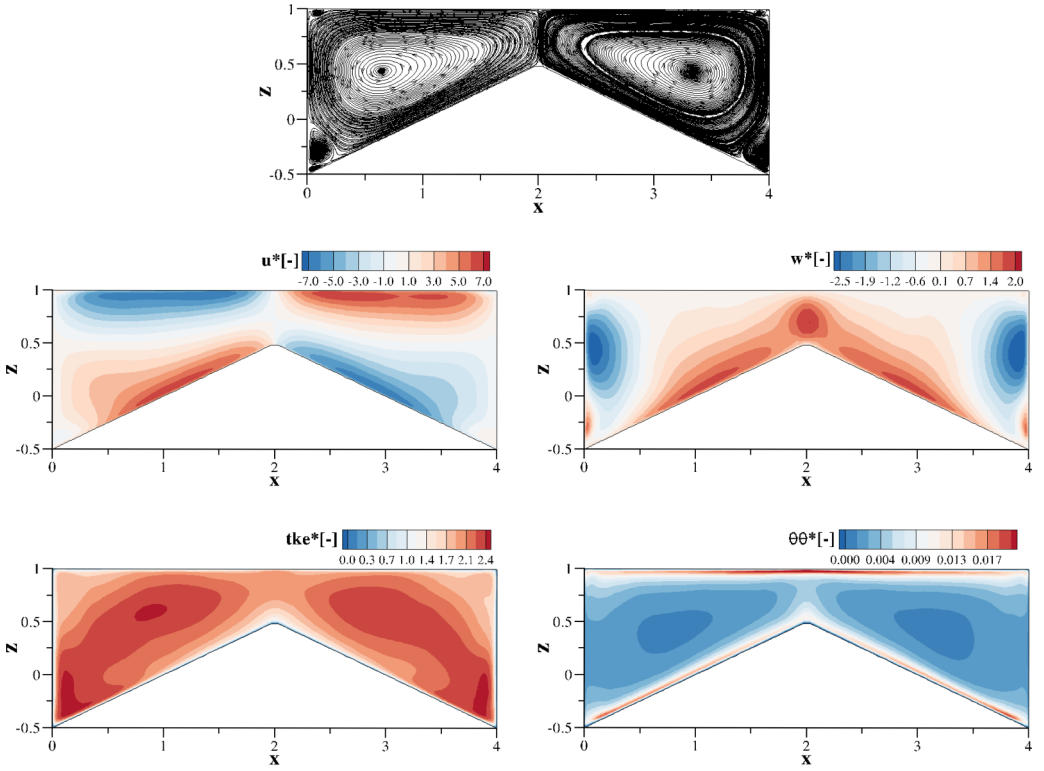

FIG. 10. (Color online) Same as in the previous figure, only now for the "Λ_0.5" configuration.

large central convective structures are again present but now accompanied with three pairs of smaller corner structures, Fig. 10 (top). The contours of the mean velocity components portray well-defined up-slope flow along the horizontal boundaries for both configurations, Figs. 9 and 10 (middle left). The characteristic down-draft (for "V_0.75") or up-draft (for "Λ_0.5") occupies the central part of the enclosure, Figs. 9 and 10 (middle right). The contours of the turbulent kinetic energy for the "V_0.75" configuration indicate three distinct regions of high intensity of velocity fluctuations: one in the upper-central location in the proximity of the top boundary where deattachment of the vertical down-draft is located and two zones located between the inclined bottom and top walls, Figs. 9 (bottom left). Similarly, two central zones of a high turbulent kinetic energy are also observed for the "Λ_0.5" configuration, with the addition of two smaller zones positioned in the enclosure lower corners, Fig. 10 (bottom left). The contours of the temperature variance exhibit a different behavior. For both configurations, the highest intensity of temperature fluctuations is in the proximity of the thermally active surfaces, with local peaks at the impingement regions, Figs. 9 and 10 (bottom right).

The vertical profiles of the first and second moments of velocity and temperature fields in the centerline of the enclosure [i.e., along the $(x/L = 2,\ y/W = 2)$ line, the "2-2" location in Fig. 1 (middle)] for $\mathrm{Ra} = 10^7$ and 10^9 are shown in Figs. 11 and 12. In contrast to the standard case (i.e., "F" configuration), various inclinations produce asymmetrical distributions of the mean temperature, Figs. 11 (top left) and 11 (bottom left). Whereas the mean temperature is always above the neutral referent value of $(\theta^* = 0.5)$ for the "Λ_0.5" configuration, the "V-type" inclinations exhibit contrasting trends for different Ra. The colder (below the referent value) profiles are obtained for all "V-type" inclinations at $\mathrm{Ra} = 10^7$, confirming the dominance of the vertical downdraft in the central part of the enclosure. In contrast, at $\mathrm{Ra} = 10^9$, all mean temperature profiles are above the referent value, indicating different behaviors. This trend is produced by a relatively strong spanwise-oriented (in the y direction) mean flow (or so-called background wind, similarly observed in Refs. [10,39,41,44]). The imprints of the wind are clearly observed by comparing the profiles of the v-velocity component for $\mathrm{Ra} = 10^7$ and 10^9, Figs. 11 (middle top) and 11 (middle bottom). While the mean v-velocity contributions are almost negligible at $\mathrm{Ra} = 10^7$, a clear spanwise-oriented looplike flow is established in the spanwise direction with positive values in the lower and negative values on the upper part of the enclosure, Fig. 11 (middle bottom). Note that the magnitude of the spanwise motion generated even exceeds values of its vertical counterpart. Later we will provide a full three-dimensional view of the flow structure which supports this finding. The profiles of the vertical w-velocity component demonstrate a gradual increase with the step-up of lower surface inclination for both Ra, Fig. 11 (right).

The vertical profiles of the normal turbulent stresses and of the turbulent heat flux are given in Fig. 12. Again, apart from configuration with flat walls ("F"), all inclined configurations exhibit asymmetrical behavior for the horizontal component

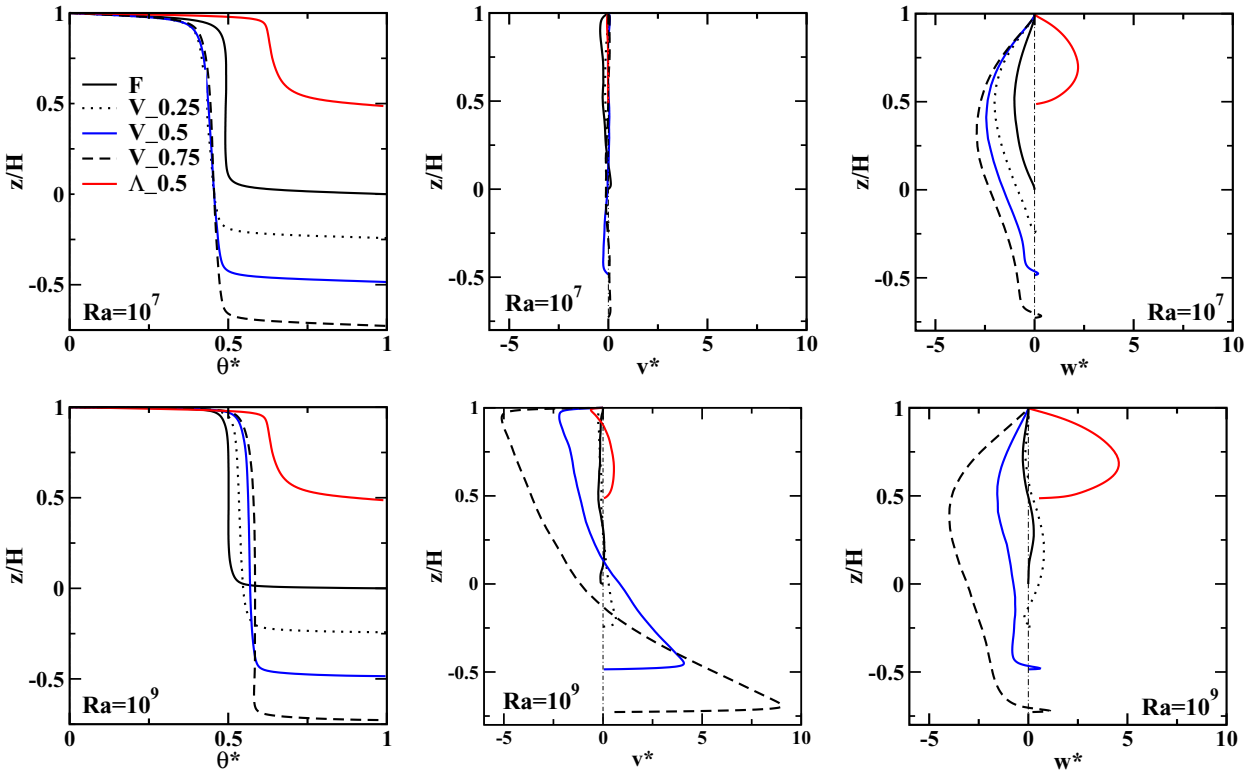

FIG. 11. (Color online) The vertical profiles of the time-averaged nondimensional vertical $(w^* = \overline{w}/u_0)$ (left), spanwise $(v^* = \overline{v}/u_0)$ (middle) velocity, and temperature $(\theta^* = \overline{\theta}/\Delta\theta)$ (right) extracted along the $x/L = 2$ and $y/W = 2$ lines (the 2-2 location in Fig. 1) for different configurations and different Ra [10^7 (top) and 10^9 (bottom)].

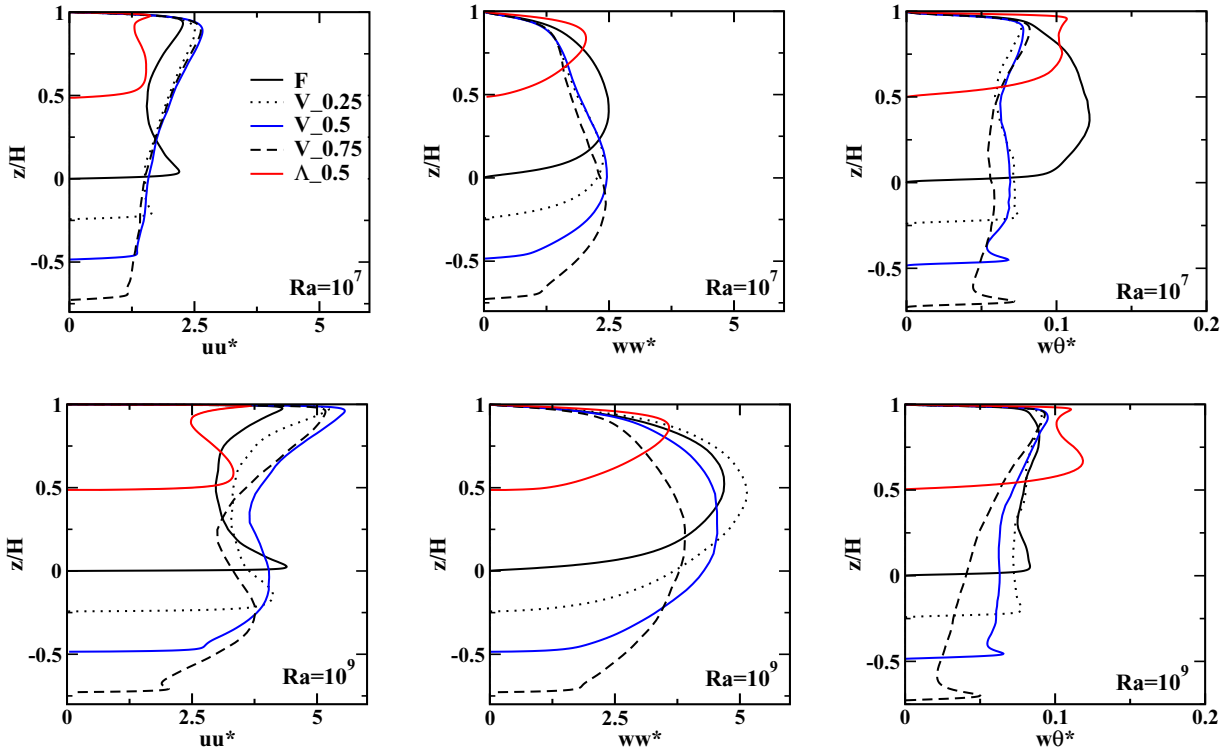

FIG. 12. (Color online) Same as in Fig. 11 only now for the horizontal ($uu^* = \sqrt{\overline{uu}}/u_0$) and vertical ($ww^* = \sqrt{\overline{ww}}/u_0$) turbulent stresses as well as of the vertical turbulent heat flux component [$w\theta^* = \overline{w\theta}/(u_0\Delta\theta)$].

of the turbulent stress, Fig. 12 (left). Note that the peak values in the proximity of the top surface are almost identical for all V-type inclinations for both Ra. With a Ra increase, the second peak in the proximity of the bottom surface is generated, Fig. 12 (bottom left). In contrast to the horizontal component of the turbulent stress, its vertical component reaches the highest value in the central part of the domain, Fig. 12 (middle). Now, for the V types of inclinations, distributions switch from asymmetrical for Ra $= 10^7$ (with peaks in the proximity of the lower boundary) to fully symmetrical for Ra $= 10^9$. Finally, the vertical turbulent heat flux profiles for the V-type inclinations have two characteristic peaks in the near-wall regions, in contrast to a single peak in the center of domain for flat-walls configuration, Fig. 12 (right).

To investigate possible changes of the boundary layer structure in the proximity of the top cold surface, we extract the vertical profiles of the temperature variance along the ($y/W = 2$ and $x/L = 1$) line, Fig. 13. For a given Ra, the distance from the upper wall where the temperature variance reaches its peak value is practically identical for all inclinations. This

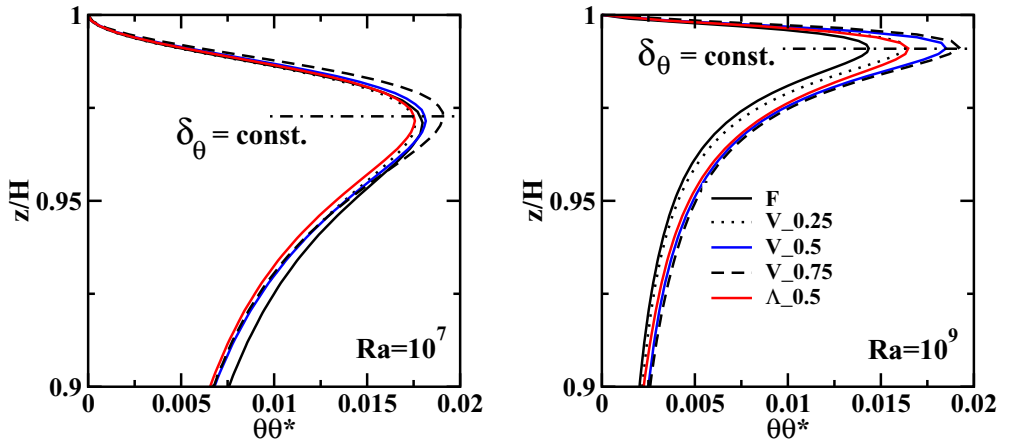

FIG. 13. (Color online) The vertical profiles of the nondimensional temperature variance ($\theta\theta^* = \sqrt{\overline{\theta^2}}/\Delta\theta$) extracted along $x/L = 1$ and $y/W = 2$ line (the $1-1$ location in Fig. 1) for different configurations and different Ra $= 10^7$ (left) and 10^9 (right). The $\delta_\theta = \text{const}$ line indicates the thickness of the thermal boundary layer.

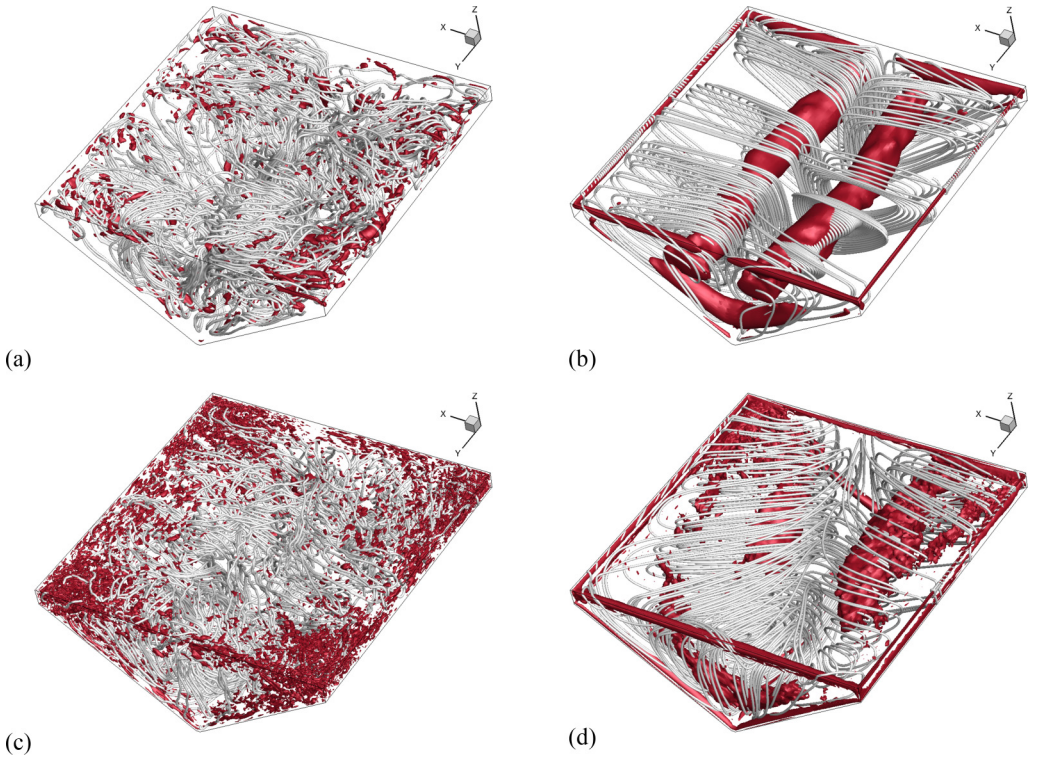

FIG. 14. (Color online) The "V_0.75" configuration: instantaneous [(a) and (c)] and long-term time-averaged [(b) and (d)] stream traces (gray tubes) and large coherent structures identified as isosurfaces of the q-parameter, where $q = 10$ and 0.1 for instantaneous (left) and time-averaged (right) velocity fields, respectively, for two values of $\mathrm{Ra} = 10^7$ [(a) and (b)] and 10^9 [(c) and (d)].

indicates that there are no significant changes (laminar to turbulent transition or similar) in thermal-boundary layers along the top wall and that the heat transfer enhancement here is most probably caused by reorganization of the large-scale structures.

To identify large-scale structures, we use the q criterion, defined as the second invariant of the velocity gradient tensor, $q = -1/2(\partial u_i/\partial x_j)(\partial u_j/\partial x_i)$ [45]. The positive values of q identify regions of flow where the rotational rate prevails over the shear strain rate (vortex cores). As a representative of the "V-type" configurations, we focus the "V_075" case. For instantaneous velocity fields, the coherent structures (identified as flow regions where $q = 10$) are mostly located in proximity of the side walls for both values of Ra, Figs. 14(a) and 14(c). In contrast, for long-term averaged velocity fields, the coherent structures (identified as flow regions where $q = 0.1$) occupy the central part of cavity as well as regions in the close proximity of side walls, Figs. 14(b) and 14(d). Now spatial reorganization of these structures with Ra increase can be observed. For the $\mathrm{Ra} = 10^7$ case, the two corotating central structures are identified portraying predominantly two-dimensional flow organization (clearly visible from distributions of the stream traces, which are shown as gray tubes), Fig. 14(b). For $\mathrm{Ra} = 10^9$, two central coherent structures are still present, but they do not extend along the entire spanwise dimension (along the y-coordinate direction) of the enclosure, Fig. 14(d). This confirms effects of the long-term averaged spanwise velocity and breaking of the two-dimensional flow structures (which also can be seen from the stream traces). Such three-dimensional mixing (superimposed up-slope and down-slope and streamwise wind) enhances the wall heat transfer. Even more complex convective structures are identified in the "Λ_0.5" configuration, Fig. 15. Now the central part of the enclosure is less populated with instantaneous coherent structures, as illustrated in Figs. 15(a) and 15(c). For the long-time averaged velocity fields, for both Ra, we identify the four central structures, six smaller structures aligned with the spanwise side walls and also six coherent structures aligned with the front and back walls, Figs. 15(b) and 15(d). Again, for higher Ra, the significantly stronger background wind in the spanwise direction can be seen (note the orientation of the stream traces), Figs. 15(b) and 15(d).

IV. SUMMARY AND CONCLUSIONS

We performed numerical simulations of turbulent thermal convection of air in the enclosure with different topologies of the lower surface ("V"- or "Λ"-shaped configurations). The lower and upper surfaces were kept at constant temperatures, while the side boundaries were adiabatic. We studied an intermediate range of Ra ($10^6 \leqslant \mathrm{Ra} \leqslant 10^9$) and demonstrated that a significant heat-transfer augmentation (up to 32%) can be achieved. This heat-transfer enhancement was the result of combined effects of the enlargement of the heated surface and of the spatial reorganization of the large-scale structures. The flow reorganization (compared to the neutral case with flat walls) starts as a well-defined up-slope mean motion (along the lower surface) and with Ra increase is completed with generation of a strong background wind in the spanwise

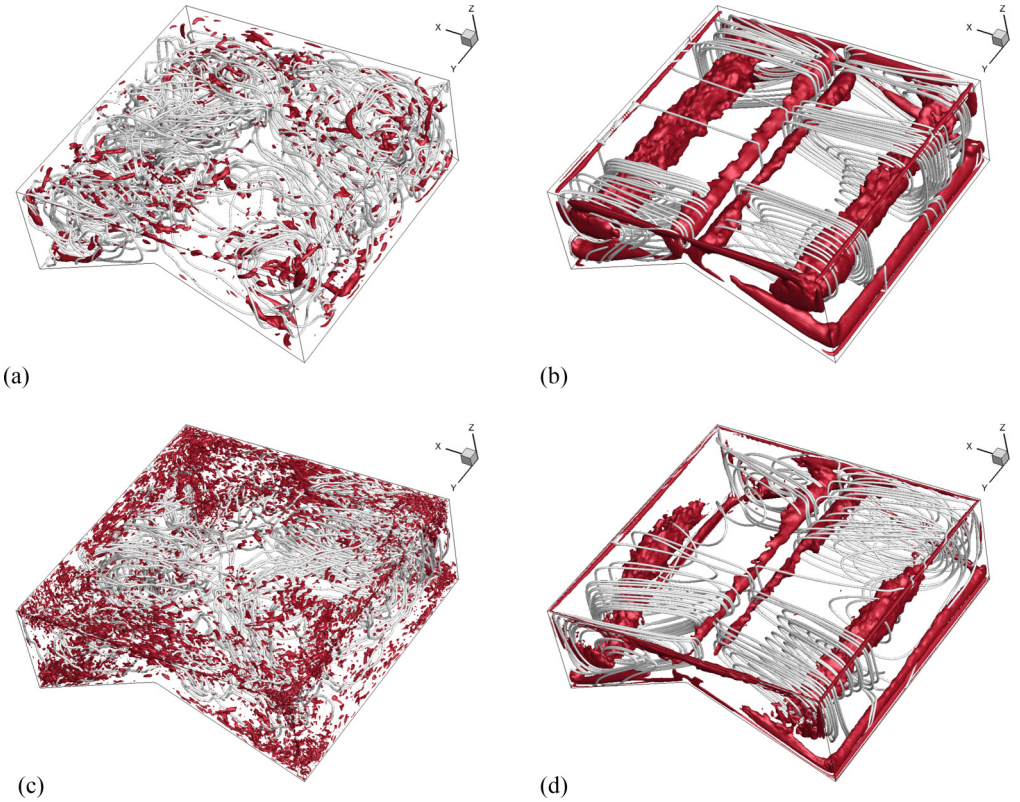

FIG. 15. (Color online) The "A_0.5" configuration: instantaneous [(a) and (c)] and long-term time-averaged [(b) and (d)] stream traces (gray tubes) and large coherent structures identified as isosurfaces of the q parameter, where $q = 10$ and 0.1 for instantaneous (left) and time-averaged (right) velocity fields, respectively, for two values of $\mathrm{Ra} = 10^7$ [(a) and (b)] and 10^9 [(c) and (d)].

direction. We conclude that this "passive" control of the heat transfer can be effectively and relatively easily applied in numerous practical applications dealing with efficient cooling of electric devices.

ACKNOWLEDGMENTS

We gratefully acknowledge NWO Physical Sciences, who supported access to supercomputing facilities at the SURFsara, eScience Center in Amsterdam, The Netherlands [46].

[1] E. D. Siggia, Annu. Rev. Fluid Mech. **26**, 137 (1994).
[2] S. Grossmann and D. Lohse, J. Fluid Mech. **407**, 27 (2000).
[3] L. P. Kadanoff, Phys. Today **54**(8), 34 (2001).
[4] K. Hanjalić, Annu. Rev. Fluid Mech. **34**, 321 (2002).
[5] G. Ahlers, G. Siegfied, and D. Lohse, Rev. Mod. Phys. **81**, 503 (2009).
[6] D. Lohse and K.-Q. Xia, Annu. Rev. Fluid Mech. **42**, 335 (2010).
[7] O. Shishkina, R. J. A. M. Stevens, S. Grossmann, and D. Lohse, New J. Phys. **12**, 075022 (2010).
[8] R. du Puits, L. Li, C. Resagk, A. Thess, and C. Willert, Phys. Rev. Lett. **112**, 124301 (2014).
[9] A. Nikolaenko, E. Brown, D. Funfschilling, and G. Ahlers, J. Fluid Mech. **523**, 251 (2005).
[10] R. du Puits, C. Resagk, and A. Thess, Phys. Rev. E **75**, 016302 (2007).
[11] Q. Zhou, B.-F. Liu, C.-M. Li, and B.-C. Zhong, J. Fluid Mech. **710**, 260 (2012).
[12] S. Ciliberto, S. Cioni, and C. Laroche, Phys. Rev. E **54**, R5901 (1996).
[13] K.-Q. Xia and S.-L. Lui, Phys. Rev. Lett. **79**, 5006 (1997).
[14] Y. Shen, P. Tong, and K.-Q. Xia, Phys. Rev. Lett. **76**, 908 (1996).
[15] P.-E. Roche, B. Castaing, B. Chabaud, and B. Hébral, Phys. Rev. E **63**, 045303(R) (2001).
[16] G. Stringano, G. Pascazio, and R. Verzicco, J. Fluid Mech. **557**, 307 (2006).
[17] J.-Q. Zhong, R. J. A. M. Stevens, H. J. H. Clercx, R. Verzicco, D. Lohse, and G. Ahlers, Phys. Rev. Lett. **102**, 044502 (2009).
[18] S. Kenjereš, Phys. Rev. E **78**, 066309 (2008).
[19] S. Kenjereš, Theor. Comput. Fluid Dyn. **23**, 471 (2009).
[20] S. Kenjereš, Phys. Fluids **23**, 015103 (2011).
[21] J. Salort, O. Liot, E. Rusaouen, F. Seychelles, J.-C. Tisserand, M. Creyssels, B. Castaing, and F. Chillà, Phys. Fluids **26**, 015112 (2014).
[22] S. Wagner and O. Shishkina, J. Fluid Mech. **763**, 109 (2015).
[23] S.-D. Huang, M. Kaczorowski, R. Ni, and K.-Q. Xia, Phys. Rev. Lett. **111**, 104501 (2013).
[24] U. Schumann, Q. J. R. Meteor. Soc. **116**, 637 (1990).
[25] S. Kenjereš and K. Hanjalić, J. Turbul. **3**, 1 (2002).
[26] F. K. Chow, A. P. Weigel, R. L. Street, M. W. Rotach, and M. Xue, J. Appl. Meteor. Climatol. **45**, 63 (2006).

[27] B. Zhou and F. K. Chow, J. Atmos. Sci. **70**, 3262 (2013).
[28] J. H. Ferziger and M. Perić, *Computational Methods for Fluid Dynamics*, 3rd ed. (Springer, Berlin, Heidelberg, 2002).
[29] A. W. Vreman, Phys. Fluids **16**, 3670 (2004).
[30] T. M. Eidson, J. Fluid Mech. **158**, 245 (1985).
[31] S. Kenjereš and K. Hanjalić, Int. J. Heat Fluid Fl. **27**, 800 (2006).
[32] S. Kenjereš and K. Hanjalić, Phys. Rev. Lett. **98**, 104501 (2007).
[33] S. Kenjereš and K. Hanjalić, New J. Phys. **9**, 306 (2007).
[34] S. Kenjereš, Int. J. Multiscale Com. **7**, 545 (2009).
[35] S. A. Theerthan and J. H. Arakeri, Phys. Fluids **12**, 884 (2000).
[36] Q. Zhou, C. Sun, and K.-Q. Xia, Phys. Rev. Lett. **98**, 074501 (2007).
[37] R. M. Kerr, J. Fluid Mech. **310**, 139 (1996).
[38] S. Kenjereš and K. Hanjalić, Phys. Rev. E **66**, 036307 (2002).
[39] S. Wagner, O. Shishkina, and C. Wagner, J. Fluid Mech. **697**, 336 (2012).
[40] B. Gayen, G. O. Hughes, and R. W. Griffiths, Phys. Rev. Lett. **111**, 124301 (2013).
[41] M. van Reeuwijk, Ph.D. thesis, Delft University of Technology, 2007.
[42] A. Sergent, P. Joubert, and P. Le Quéré, Prog. Comp. Fluid Dyn. **6**, 40 (2006).
[43] S.-H. Peng, K. Hanjalić, and L. Davidson, J. Turbulence **7**, 1 (2006).
[44] E. Brown, A. Nikolaenko, and G. Ahlers, Phys. Rev. Lett. **95**, 084503 (2005).
[45] J. C. R. Hunt, A. A. Wray, and P. Moin, Center for Turbulence Research Report CTR-S88, 193 (1988).
[46] High Performance Computing and data infrastructure for science and industry, SURFsara, Amsterdam, The Netherlands, www.surfsara.nl.